Shape Estimation of Transparent Objects by Using Inverse Polarization Ray Tracing

Daisuke Miyazaki, *Member*, *IEEE*, and Katsushi Ikeuchi, *Fellow*, *IEEE*

Abstract—Few methods have been proposed to measure three-dimensional shapes of transparent objects such as those made of glass and acrylic. In this paper, we propose a novel method for estimating the surface shapes of transparent objects by analyzing the polarization state of the light. Existing methods do not fully consider the reflection, refraction, and transmission of the light occurring inside a transparent object. We employ a polarization raytracing method to compute both the path of the light and its polarization state. Polarization raytracing is a combination of conventional raytracing, which calculates the trajectory of light rays, and Mueller calculus, which calculates the polarization state of the light. First, we set an initial value of the shape of the transparent object. Then, by changing the shape, the method minimizes the difference between the input polarization data and the rendered polarization data calculated by polarization raytracing. Finally, after the iterative computation is converged, the shape of the object is obtained. We also evaluate the method by measuring some real transparent objects.

Index Terms—Polarization, raytracing, shape-from-X, transparency, Mueller calculus.

---

1 INTRODUCTION

IN the field of computer vision, few methods have been proposed for estimating the shape of transparent objects because of the difficulty of dealing with mutual reflection, which is the phenomenon that the light not only reflects at the surface of the transparent object but also transmits into the object and causes multiple reflections and transmissions inside it. In this paper, we use the term "interreflection" for such internal reflection. This paper presents a novel method for estimating the surface shape of transparent objects by analyzing the polarization of transparent objects.

The methods for estimating the shape of transparent objects can be divided into two types: geometric methods and photometric methods. Geometric methods analyze the position and the direction of the light ray, whereas photometric methods analyze the physical state of the light.

Considerable previous research has been conducted on geometric methods. Murase [20] estimated the shape of a water surface by analyzing the undulation of the surface, and Morris and Kutulakos [19] extended this method to determine the shape of a water surface by observing the water from two views. The purpose of our research, however, is to measure still objects. Hata et al. [8] estimated the surface shape of transparent objects by analyzing the deformation of the light projected onto the transparent objects. Their method is implemented by a genetic algorithm that attempts to find the minimum cost function probabilistically, whereas our method finds the minimum cost function deterministically. Ben-Ezra and Nayar [3] estimated the parameterized surface shapes of transparent objects by multiple viewpoints, whereas our method estimates a nonparameterized surface

shape; thus, our method is useful for object recognition. Kutulakos and Steger [15] estimated both the depth and the surface normal of transparent objects by multiple viewpoints and multiple light sources. They have to move the light sources around the object, whereas our proposed method does not need to move the light sources, since it wholly surrounds the object.

Photometric methods are all based on polarization analysis. Polarization is a phenomenon in which the light oscillates in one direction [4], [9]. Recent research in estimating the shape of an object by using polarization is impressive [1], [2], [14], [17], [22], [28]. Saito et al. [23] and Miyazaki et al. [16], [18] estimated the surface shape of transparent objects by analyzing the polarization phenomenon. Geometric methods compute the shape by analyzing the refraction of the light ray; thus, they cannot measure a thin transparent object, which causes less refraction. In order to estimate the orientation of a thin object, we have to analyze the reflection instead of refraction, and the photometric methods consider reflections. Our previous methods [16], [18] did not consider interreflection; they assumed that the light would reflect at the surface only once. They found that there is an ambiguity problem for estimating the surface normal of the object from polarization information. Two possible zenith angles are produced from the degree of polarization (DOP): one is correct and the other is incorrect. The method proposed in this paper does not solve this ambiguity problem but considers interreflection, which provides a more precise shape than our previous methods. The proposed method iteratively updates the shape of the object from a given initial shape.

In this paper, a forward-facing surface of the transparent object is called a front surface and an object surface facing away from the camera is called a back surface. Our proposed method estimates the front surface shape of the transparent object by using a method called polarization raytracing, which simulates the interreflection, under the assumptions that the refractive index, the shape of the back surface, and the illumination distribution are given.

- *The authors are with the Ikeuchi Laboratory, 3rd Department, Institute of Industrial Science, The University of Tokyo, 4-6-1 Komaba, Meguro-ku, Tokyo, Japan 153-8505. E-mail: {miyazaki, ki}@cvl.iis.u-tokyo.ac.jp.*
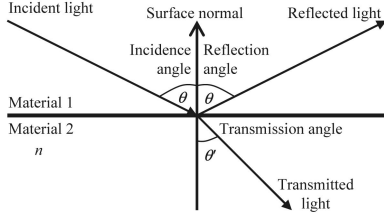
Fig. 1. Reflection, refraction, and transmission.

The rest of the paper is organized as follows: First, Section 2 presents assumptions for our method. In Section 3, we describe the theoretical background of the polarization raytracing method. In Section 4, we explain our estimation method, which solves the inverse problem of the polarization raytracing method. We prove the convergence of our method in Section 5. Our measurement results are shown in Section 6, and our conclusions are presented in Section 7.

2 ASSUMPTIONS

There are several assumptions we use to successfully apply the method:

1. The object is observed as an orthographic projection to the image plane of the camera.
2. The object is transparent and solid.
3. The refractive index is known and constant for any part of the object, implying that the method is not applicable to birefringent media.
4. The object's surface is optically smooth (not microscopically rough).
5. The object's surface is geometrically smooth and closed (C^1 surface). This assumption and the next imply that the surface normal can be calculated by differentiating the height of the object's surface.
6. No self-occlusion exists. There is no "jump" in the height of the object surface.
7. The entire front surface is included in the camera field of view.
8. The back surface shape is known.
9. The initial value of the front surface is given a priori. This value can be given, for example, by a human operator or by previous methods [16], [18].
10. The polarization state and the intensity of the illumination distribution should be known. We used uniform illumination distribution in our experiments. Therefore, we hereafter assume that the light illuminating the object is unpolarized, uniform, and known. In addition, our experimental setup illuminates the front surface more intensely than the back surface; thus, this condition is also used in this paper.

3 POLARIZATION RAYTRACING

3.1 Calculation of Light Path

Fig. 1 describes the light reflected and transmitted between material 1 and material 2. Materials 1 and 2 may be, respectively, the air and the transparent object, and vice versa. Incidence angle, reflection angle, and transmission angle are defined in Fig. 1. We assume that the surface of transparent objects is optically smooth; thus, the incidence

angle is equal to the reflection angle. The transmission angle is related to the incidence angle with Snell's law [4], [9]

$$\sin \theta = n \sin \theta', \qquad (1)$$

where θ is the incidence angle, θ' is the transmission angle, and n is the ratio of the refractive index of material 2 to that of material 1. The plane of incidence (POI) is a plane that includes the surface normal direction, the incident light direction, the reflected light direction, and the transmitted light direction.

3.2 Calculation of Intensity

The intensity ratio of reflected light to incident light is called intensity reflectivity R and the intensity ratio of transmitted light to incident light is called intensity transmissivity T. Subscripts $\parallel$ and $\perp$ represent the components parallel and perpendicular to POI, respectively. Parallel and perpendicular components of intensity reflectivity and intensity transmissivity for dielectric transparent material are given as follows [4], [9]:

$$R_\parallel = \frac{\tan^2(\theta - \theta')}{\tan^2(\theta + \theta')}, \qquad (2)$$

$$R_\perp = \frac{\sin^2(\theta - \theta')}{\sin^2(\theta + \theta')}, \qquad (3)$$

$$T_\parallel = \frac{\sin 2\theta \sin 2\theta'}{\sin^2(\theta + \theta') \cos^2(\theta - \theta')}, \qquad (4)$$

$$T_\perp = \frac{\sin 2\theta \sin 2\theta'}{\sin^2(\theta + \theta')}. \qquad (5)$$

If an incidence angle is larger than the critical angle, then the light does not transmit and totally reflects. This phenomenon is called total reflection and occurs when the incidence light is inside the object. Critical angle θ_C is given as follows [4], [9]:

$$\sin \theta_c = n. \qquad (6)$$

For the total reflection, we must use $R_\parallel = R_\perp = 1$ and $T_\parallel = T_\perp = 0$.

3.3 Mueller Calculus

In this paper, we call the raytracing method that considers the polarization effect the polarization raytracing method. The algorithm of the polarization raytracing method can be divided into two parts. For the first part, the calculation of the propagation of the ray, we employ the same algorithm used in the conventional raytracing method. For the second part, the calculation of the polarization state of the light, there are four well-known methods [4], [9]: a simple calculation method using Fresnel formulas, a method using a coherence matrix, Mueller calculus, and Jones calculus. In addition, some researchers [5], [7], [25], [26], [27] proposed a method that is an extension of these methods. In this paper, we employ Mueller calculus because of its simplicity of description, along with its ease of understanding and implementation. These four methods have almost identical functions; thus, all discussions presented in this paper are also applicable to other calculi.

In Mueller calculus, the polarization state of the light is represented as Stokes vector $\mathbf{s} = (s_0, s_1, s_2, s_3)^T$. s_0 represents the intensity of the light, s_1 represents the horizontal power of
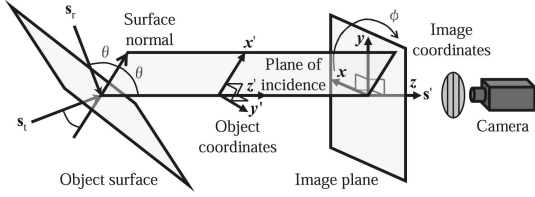
Fig. 2. Reflected and transmitted light observed by the camera.

the linear polarization, s_2 represents the +45 degrees-oblique power of the linear polarization, and s_3 represents the power of the right circular polarization. Given a certain Stokes vector $\mathbf{s}$, the normalized Stokes vector $\hat{\mathbf{s}}$ is defined as

$$\hat{\mathbf{s}} = (1, \hat{s}_1, \hat{s}_2, \hat{s}_3)^T = \left(1, \frac{s_1}{s_0}, \frac{s_2}{s_0}, \frac{s_3}{s_0}\right)^T. \tag{7}$$

The Mueller matrix, which is a 4×4 matrix, represents how the object changes the polarization state of the light.

3.4 Mueller Matrices

In this section, we present an example of calculation using Mueller calculus.

Suppose the geometrical setup when the reflected and transmitted light are observed from the camera as described in Fig. 2. In this figure, there are two coordinate systems: $x'y'z'$-coordinates and xyz-coordinates. Here, the z'-axis and the z-axis are the same. x' is included in the POI and is facing the same side as the surface normal is facing. The angle between the x'-axis and the x-axis is called the POI angle ϕ in xyz-coordinates.

In the case presented in Fig. 2, observed light is a composition of reflected light and transmitted light. The Stokes vector $\mathbf{s}'$ of the observed light is calculated as follows:

$$\mathbf{s}' = \mathbf{C}(\phi)\mathbf{D}(\delta)\mathbf{R}(\theta)\mathbf{C}(-\phi)\mathbf{s}_r + \mathbf{C}(\phi)\mathbf{T}(\theta)\mathbf{C}(-\phi)\mathbf{s}_t. \tag{8}$$

Stokes vectors of the incident light are represented as $\mathbf{s}_r$ and $\mathbf{s}_t$. $\mathbf{s}_r$ and $\mathbf{s}_t$ represent the lights that are set in the origin of the reflection and transmission, respectively. $\mathbf{C}$ is the rotation Mueller matrix and is given by [9]

$$\mathbf{C}(\phi) = \begin{pmatrix} 1 & 0 & 0 & 0 \\ 0 & \cos 2\phi & -\sin 2\phi & 0 \\ 0 & \sin 2\phi & \cos 2\phi & 0 \\ 0 & 0 & 0 & 1 \end{pmatrix}. \tag{9}$$

$\mathbf{R}$ and $\mathbf{T}$ are the reflection Mueller matrix and the transmission Mueller matrix, respectively, which are represented as follows [9]:

$$\mathbf{R} = \begin{pmatrix} (R_\parallel + R_\perp)/2 & (R_\parallel - R_\perp)/2 & 0 & 0 \\ (R_\parallel - R_\perp)/2 & (R_\parallel + R_\perp)/2 & 0 & 0 \\ 0 & 0 & \sqrt{R_\parallel R_\perp} & 0 \\ 0 & 0 & 0 & \sqrt{R_\parallel R_\perp} \end{pmatrix},$$

$$\mathbf{T} = \begin{pmatrix} (T_\parallel + T_\perp)/2 & (T_\parallel - T_\perp)/2 & 0 & 0 \\ (T_\parallel - T_\perp)/2 & (T_\parallel + T_\perp)/2 & 0 & 0 \\ 0 & 0 & \sqrt{T_\parallel T_\perp} & 0 \\ 0 & 0 & 0 & \sqrt{T_\parallel T_\perp} \end{pmatrix}. \tag{10}$$

However, if total reflection occurs, that is, if the incidence angle θ is larger than critical angle θ_C, then $\mathbf{R}$ and $\mathbf{T}$ are set to be identity matrix and zero matrix, respectively. $\mathbf{D}$ is the retardation Mueller matrix and is given as [9]

$$\mathbf{D}(\delta) = \begin{pmatrix} 1 & 0 & 0 & 0 \\ 0 & 1 & 0 & 0 \\ 0 & 0 & \cos\delta & \sin\delta \\ 0 & 0 & -\sin\delta & \cos\delta \end{pmatrix}, \tag{11}$$

where δ is the amount of the phase shift (or retardation). The phase of the reflected light shifts when total reflection occurs. Thus, for total reflection, δ in the following equation is used [4], [9]:

$$\tan\frac{\delta}{2} = \frac{\cos\theta\sqrt{\sin^2\theta - n^2}}{\sin^2\theta}. \tag{12}$$

The phase of the reflected light inverts when the incidence angle is smaller than the Brewster angle θ_B, which is given as follows [4], [9]:

$$\tan\theta_B = n. \tag{13}$$

Thus, considering (12), the value of δ used in (11) is set as follows:

$$\delta = \begin{cases} 2\arctan\frac{\cos\theta\sqrt{\sin^2\theta - n^2}}{\sin^2\theta} & (\theta \geq \theta_C) \\ 180° & (\theta \leq \theta_B) \\ 0° & \text{(otherwise)}. \end{cases} \tag{14}$$

3.5 Degree of Polarization

The polarization state of the light is calculated by observing the object with a monochrome camera, which has a linear polarizer in the front. For a certain pixel, we denote the maximum intensity observed by rotating the polarizer as I_{max} and the minimum as I_{min}. The angle of the polarizer when the minimum intensity I_{min} is observed is called the phase angle ψ. This angle is defined as the angle from the $+x$-axis to the $+y$-axis in xyz-coordinates (Fig. 2).

Because the linear polarizer is used in this research, the fourth parameter s_3 of the Stokes vector cannot be determined. The relationship between the Stokes vector $(s_0, s_1, s_2)^T$ and I_{max}, I_{min}, ψ is

$$\begin{pmatrix} s_0 \\ s_1 \\ s_2 \end{pmatrix} = \begin{pmatrix} 1 & 0 & 0 \\ 0 & \cos 2\psi & -\sin 2\psi \\ 0 & \sin 2\psi & \cos 2\psi \end{pmatrix} \begin{pmatrix} I_{max} + I_{min} \\ I_{max} - I_{min} \\ 0 \end{pmatrix}. \tag{15}$$

The DOP represents how much the light is polarized and is defined as follows:

$$\tilde{\rho} = \frac{\sqrt{s_1^2 + s_2^2 + s_3^2}}{s_0}. \tag{16}$$

However, the linear polarizer can only calculate the degree of linear polarization (DOLP):

$$\rho = \frac{I_{max} - I_{min}}{I_{max} + I_{min}} = \frac{\sqrt{s_1^2 + s_2^2}}{s_0}. \tag{17}$$

For the remainder of this paper, we refer to the DOLP calculated by (17) as DOP.

4 INVERSE POLARIZATION RAYTRACING

In this section, we introduce our method for estimating the front surface shape of a transparent object using the DOP and the phase angle as inputs under the assumption that the refractive index, the shape of the back surface, and the illumination distribution are given.

We denote the input polarization data as $\mathbf{s}_\mathcal{I}(x, y)$, where (x, y) represents the pixel position. Here, the subscript "I" represents the first letter of "input data" or "irradiance." Polarization data are represented as an image (two-dimensionally distributed data) where the Stokes vector is set for each pixel. Stokes vector has information about the DOP and the phase angle. The polarization raytracing explained in Section 3 can render the polarization data from the shape of the transparent object. We denote this rendered polarization image as $\mathbf{s}_\mathcal{R}(x, y)$. Here, the subscript "$R$" represents the first letter of "raytracing data" or "rendered data." The shape of transparent objects is represented as the height $H(x, y)$, set for each pixel. That is, the shape of the transparent object is represented in three-dimensional (3D) space, where the three axes are x, y, and H, and these are Cartesian coordinates. Heights partially differentiated by the x-axis and the y-axis are called gradients and are represented as p and q, respectively,

$$p = H_x = \frac{\partial H}{\partial x}, \quad q = H_y = \frac{\partial H}{\partial y}. \qquad (18)$$

Surface normal $\mathbf{n} = (-p, -q, 1)^T$ is represented by these gradients. That is, a surface normal is represented in two-dimensional (2D) space, where the two axes are p and q, and this space is called a gradient space.

The rendered polarization image $\mathbf{s}_\mathcal{R}(x, y)$ depends upon height and surface normal. Our problem is finding the best values to reconstruct a surface $H(x, y)$ that satisfy the following equation:

$$\mathbf{s}_\mathcal{I}(x, y) = \mathbf{s}_\mathcal{R}(x, y) \qquad (19)$$

for all pixels (x, y). We call this equation the "polarization raytracing equation" from the analogy of "image irradiance equation" used in the shape-from-shading problem described in [10], [11], [12].

A straightforward definition of the cost function, which we want to minimize, can be as follows:

$$\int \int E_1(x, y)dxdy, \qquad (20)$$

where

$$E_1(x, y) = \|\mathbf{s}_\mathcal{I}(x, y) - \mathbf{s}_\mathcal{R}(x, y)\|^2. \qquad (21)$$

Here, for calculating the cost function, we use the normalized Stokes vector, which represents only the polarization state of the light. H, p, and q must satisfy (18). Thus, we modify the cost function as follows:

$$\int \int (\lambda(x, y)E_1(x, y) + E_2(x, y))dxdy, \qquad (22)$$

where

$$E_2(x, y) = (H_x(x, y) - p(x, y))^2 + (H_y(x, y) - q(x, y))^2. \qquad (23)$$

λ is a Lagrange undetermined multiplier [6].

In order to minimize (22), we use calculus of variations [6], which is also used to solve the shape-from-shading

problem. By minimizing (22) along the p-axis, we obtain the following Euler-Lagrange differential equation [6]:

$$p(x, y) = H_x(x, y) - \frac{\lambda(x, y)}{2}\frac{\partial E_1(x, y)}{\partial p}. \qquad (24)$$

By minimizing (22) along the q-axis, we obtain the following Euler-Lagrange equation [6]:

$$q(x, y) = H_y(x, y) - \frac{\lambda(x, y)}{2}\frac{\partial E_1(x, y)}{\partial q}. \qquad (25)$$

By minimizing (22) along the H-axis, we obtain the following Euler-Lagrange equation [6]:

$$H(x, y) = \bar{H}(x, y) - \frac{p_x(x, y) + q_y(x, y)}{4} - \frac{\lambda(x, y)}{8}\frac{\partial E_1(x, y)}{\partial H}, \qquad (26)$$

where $\bar{H}(x, y)$ is a 4-neighbor average of $H(x, y)$

$$\bar{H}(x, y) = \frac{H(x+1, y) + H(x-1, y) + H(x, y+1) + H(x, y-1)}{4}. \qquad (27)$$

Each of (24) and (25) can be decomposed into two steps:

$$p^{(k)}(x, y) = H_x^{(k)}(x, y), \qquad (28)$$

$$p^{(k+1)}(x, y) = p^{(k)}(x, y) - \lambda_1^{(k+1)}(x, y)\frac{\partial E_1^{(k)}(x, y)}{\partial p}, \qquad (29)$$

$$q^{(k)}(x, y) = H_y^{(k)}(x, y), \qquad (30)$$

$$q^{(k+1)}(x, y) = q^{(k)}(x, y) - \lambda_2^{(k+1)}(x, y)\frac{\partial E_1^{(k)}(x, y)}{\partial q}. \qquad (31)$$

Here, λ_1 and λ_2 are scalar values that are determined for each pixel and for each iteration step. Superscript (k) represents the iteration number. Equation (26) can also be decomposed into two steps

$$H^{(k+\frac{1}{2})}(x, y) = \bar{H}^{(k)}(x, y) - \frac{p_x^{(k+1)}(x, y) + q_y^{(k+1)}(x, y)}{4}, \qquad (32)$$

$$H^{(k+1)}(x, y) = H^{(k+\frac{1}{2})}(x, y) - \lambda_3^{(k)}(x, y)\frac{\partial E_1^{(k)}(x, y)}{\partial H}. \qquad (33)$$

Here, λ_3 is a scalar value that is determined for each pixel and for each iteration step.

Equation (33) minimizes the error value E_1 along the H-axis; however, this is already minimized in (29) and (31) along the p-axis and the q-axis. Therefore, we do not have to use (33). In this research, we assume the surface is C^1, that is, the surface is differentiable (Assumptions 5 and 6 in Section 2); thus, we must estimate the gradients using (29) and (31). Although we can additionally use (33), the calculation will be redundant if we use it. Also, we have found that the cost function E_1 smoothly changed when the surface normal changed, but it did not smoothly change when the height changed. Please refer to Fig. 8 (Section 6.2.2) for the cost function when the height changed. For these reasons, we chose to use only p and q instead of H for minimizing the cost function. Consequently, instead of (32) and (33), we use the following formula to update the height:

$$H^{(k+1)}(x, y) = \bar{H}^{(k)}(x, y) - \frac{p_x^{(k+1)}(x, y) + q_y^{(k+1)}(x, y)}{4}. \qquad (34)$$
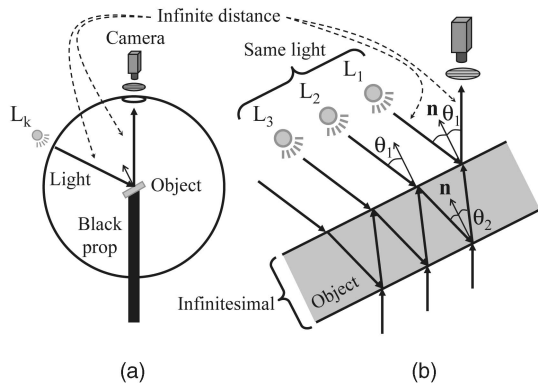
Fig. 3. Thin planar transparent object: (a) long-shot and (b) close-up.

The algorithm goes as follows:

1. First, we set initial values of the shape $H(x, y)$ for each point of the front surface.
2. Next, $p(x, y)$ and $q(x, y)$ are calculated by (28) and (30).
3. Then, we solve (29) and (31). $\lambda_1(x, y)$ and $\lambda_2(x, y)$ are determined by Brent's method [21] in order to update $p(x, y)$ and $q(x, y)$ so that the cost function $E_1(x, y)$ will be smaller. Brent's method finds the local minimum along one-dimensional space like the golden section search [21].
4. After computing $p(x, y)$ and $q(x, y)$ at every pixel, we solve (34) by the relaxation method [21] to determine the height $H(x, y)$. Ikeuchi [13] solved the relaxation problem by using the Jacobi method [21], whereas Horn [11] solved it by means of the successive overrelaxation method [21]. We use the alternating-direction implicit method [21] instead to increase the speed of computation.

The front surface shape of the transparent object is estimated by an iterative computation, where each step of iteration solves (28), (29), (30), (31), and (34), and the iteration stops when (20) is minimized.

5 CONVERGENCE

5.1 Planar Object Case

In this section, we discuss the convergence of our method. We use a virtual transparent planar object, as illustrated in Fig. 3, for discussing the convergence of our method. Both sides of the planar object are set to be parallel. Assumptions suggested in Section 2 are satisfied for this analysis. Here, we discuss the case that only one side of the object is illuminated by uniform unpolarized light sources from every direction. The camera is set on the same side as the light sources. The other side of the object is placed on a completely black pedestal.

In Fig. 3b, the light ray L_1 is reflected at the object surface and observed by the camera. The light ray L_2 is first transmitted into the object, next reflected inside the object, then transmitted out from the object and, finally, observed by the camera. The same process also applies to the other light rays and we denote the kth light ray as L_k. For simplicity of the analysis, we set either one of the following assumptions:

1. We assume that both the distance between the camera and the object and the distance between the object and the light source are infinite. Therefore, all of the light rays L_k mathematically coincide in the infinite far distance.
2. We assume that the thickness of the object is infinitesimal. Since the light rays L_k are parallel, these light rays will mathematically coincide.
3. We assume that the light source distribution is uniform. That is, even if the light rays L_k are different, their properties are the same.

Since it is impossible to depict the infinite distance and the infinitesimal thickness, we express the setup with finite distance and thickness in Fig. 3. All of the above three assumptions indicate that the light rays have same intensity; thus, we just simply assume that all of the light rays L_k have the same intensity. In addition, we set all of the light sources as unpolarized lights. Therefore, we represent the Stokes vector of all light sources as $\mathbf{L}_k = (1, 0, 0, 0)^T$.

The angle θ_1 is the reflection angle in the air, and the angle θ_2 is the reflection angle in the object. From (1), the following equation holds:

$$\sin \theta_1 = n \sin \theta_2, \qquad (35)$$

where n is the refractive index of the object.

The Stokes vector of the observed light $\mathbf{I}$ will be

$$\mathbf{I} = \mathbf{R}\mathbf{L}_1 + \sum_{k=2}^{K} \mathbf{T}\mathbf{R}^{2k-3}\mathbf{T}\mathbf{L}_k, \qquad (36)$$

where $\mathbf{R}$ and $\mathbf{T}$ are given in (10). The following properties hold in this case:

$$R_\parallel + T_\parallel = 1, \qquad R_\perp + T_\perp = 1, \qquad (37)$$

$$R(\theta_1; n) = R\left(\theta_2; \frac{1}{n}\right), \quad T(\theta_1; n) = T\left(\theta_2; \frac{1}{n}\right), \qquad (38)$$

$$0 \leq R < 1, \qquad (39)$$

$$R + R^3 + \cdots + R^{2K-3} = \frac{R(1 - R^{2K-2})}{1 - R^2}, \qquad (40)$$

$$\mathbf{R}^m =$$
$$\begin{pmatrix} (R_\parallel^m + R_\perp^m)/2 & (R_\parallel^m - R_\perp^m)/2 & 0 & 0 \\ (R_\parallel^m - R_\perp^m)/2 & (R_\parallel^m + R_\perp^m)/2 & 0 & 0 \\ 0 & 0 & \sqrt{R_\parallel^m R_\perp^m} & 0 \\ 0 & 0 & 0 & \sqrt{R_\parallel^m R_\perp^m} \end{pmatrix}.$$
$$(41)$$

K should be set as $K \to \infty$; thus, in this specific case, by using (37), (38), (39), (40), and (41), (36) will be reformulated as

$$\mathbf{I} = (s_0, s_1, s_2, s_3)^T = (s_0, s_1, 0, 0)^T, \qquad (42)$$

$$s_0 = \frac{1}{1 + R_\parallel} R_\parallel + \frac{1}{1 + R_\perp} R_\perp, \qquad (43)$$

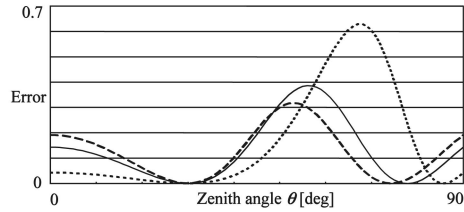$$s_1 = \frac{1}{1 + R_\parallel} R_\parallel - \frac{1}{1 + R_\perp} R_\perp. \qquad (44)$$

Fig. 4. Error value for planar object. A dashed line, solid line, and dotted line are the case for $n = 1.33$, 1.5, and 2.42, respectively.

Note that Schechner et al. [24] also analyzed the polarization effect of a transparent planar object.[1]

In Fig. 4, we have plotted the value of the cost function E_1, defined in Section 4, as a function of the reflected angle θ_1. Here, we set the true angle as 30 degrees. The vertical axis represents the value of the cost function, and the horizontal axis represents the angle. The refractive indices are set as 1.33, 1.5, and 2.42 for dashed line, solid line, and dotted line, respectively. Note that the cost function E_1 is calculated from the normalized Stokes vector; thus, the error values for the refractive indices do not differ greatly in spite of the difference in observed intensities.

The error is zero at 30 degrees and the error is greater than zero around 30 degrees. Also, the error curve is wholly smooth. Evidently, we can insist that our minimization method can successfully estimate the true angle if we set the initial value near the true value. However, there is another valley around 74 degrees, 78 degrees, and 86 degrees for $n = 1.33$, $n = 1.5$, and $n = 2.42$, respectively. To avoid such local minimum, we must set the initial value properly. Moreover, the error value is zero at such minimum points. Therefore, we cannot adopt a strategy to search the solution globally. This bimodality is caused by the ambiguity problem discussed in our previous paper [16], [18]. Our previous method solved this ambiguity problem, though we could not deal with the interreflection of transparent objects at that time, whereas the main purpose of this paper is to deal with the interreflection. Such ambiguity always appears whether we consider the interreflection or not and always appears for any refractive indices.

5.2 General Case

The shape of the object can vary arbitrarily, and it is difficult to express arbitrary shapes in analytic formulas. It is also difficult to express the raytracing algorithm in analytic formulas for general cases. Therefore, we conclude that we cannot discuss the convergence of our method for general shapes analytically. It can only be argued empirically, and some experimental results are provided in Section 6.

6 MEASUREMENT RESULT

6.1 Experimental Setup

6.1.1 Acquisition System

For obtaining polarization data, we developed an acquisition system that we named "Cocoon" (Fig. 5). The target object is

<hr/>

1. The DOP is calculated by s_1/s_0 in our case, and the same function can be derived by substituting (1) in [24] into the first formula of (2) in [24]. This function is plotted in the upper part in Fig. 2 in [24]. In that figure, solid curve represents the DOP without considering the interreflection, and the dashed curve represents the DOP, considering the interreflection.
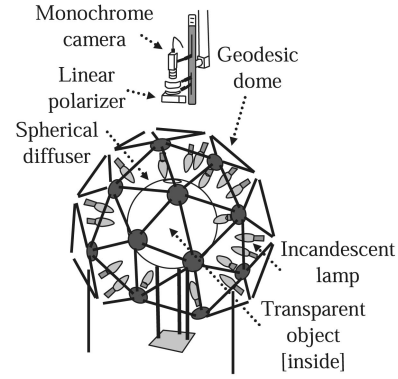

Fig. 5. Acquisition system "cocoon."

set inside the center of a plastic sphere whose diameter is 35 cm. This plastic sphere is illuminated by 36 incandescent lamps that are almost uniformly distributed spatially around the plastic sphere by a geodesic dome. The plastic sphere diffuses the light that comes from the light sources, and it behaves as a spherical light source, which illuminates the target object from every direction. The target object is observed by a monochrome camera from the top of the plastic sphere, which has a hole on the top whose diameter is 6 cm. A linear polarizer is set in front of the camera. The camera, object, and light sources are fixed. From four images taken by rotating the polarizer at 0 degrees, 45 degrees, 90 degrees, and 135 degrees, we calculate I_{max}, I_{min}, and ψ (Section 3.5) by the least squares method.

6.1.2 Extended Light Source

Thanks to the spherical diffuser, which provides a uniform illumination, we can analyze the reflected light in a large area of the object's surface. Also, if the illumination is not uniform and the illumination is a mixture of bright light and dark light, it will become difficult to set the appropriate dynamic range of the camera.

When the light of an incandescent lamp penetrates the white plastic diffuser, the light will be unpolarized while randomly scattered inside the diffuser. The distance between the diffuser and the object is large compared with the size of the object. Therefore, the spherical diffuser provides an unpolarized light.

We obtained the variance of DOP and intensity of the spherical diffuser a priori. We put the polarizer-mounted camera inside the spherical diffuser and measured the equator of the sphere in three directions that are 120 degrees apart. The same field of view of the camera is used in this measurement as that used in observing the object. The average DOP of all the pixels was 0.0013, where the variance was 0.0000041. The variance of the intensity was 0.000013 when we set the average intensity as 1.

Since we know the size of the sphere and that of the hole on top of the sphere, we know that the size of the hole is 19.7 degrees. We implemented our software under the condition that the illumination is uniform and unpolarized though the light does not come from the hole on top of the sphere.

6.1.3 Intensity of Illumination

We put the target object on a black pipe so that the light will not reflect behind the object. However, a small amount of
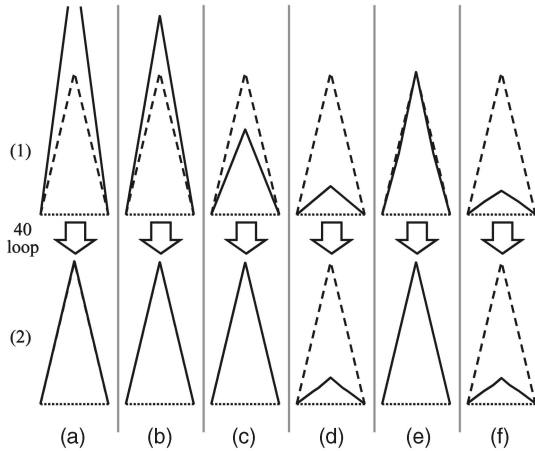
Fig. 6. Simulation result of a triangle: (1) initial state, (a), (b), (c), and (d) True height scaled by 1.8, 1.4, 0.6, 0.2, respectively, (e) and (f) two solutions caused by the ambiguity problem; (2) estimated result after 40 iterations.

Fig. 7. Simulation result of a hemisphere: (a) no noise is added and (b) Gaussian noise is added.

light, which we denote as "background radiation" in this paper, is still emitted from the cavity of the black pipe. The measurement results are affected by this background radiation. Fortunately, the background radiation was found to be uniform and unpolarized in the preliminary experiment. Therefore, we computed the polarization raytracing algorithm by considering the background radiation, assuming that it is uniform and unpolarized with its intensity known.

The intensity of the background radiation is determined indirectly from observation. We observe a hemispherical acrylic transparent object, whose refractive index is 1.5 and diameter is 30 mm. From the known geometry, we have iteratively computed the intensity by using a modified version of our algorithm. The original algorithm calculates the shape from the illumination; however, here, we calculate the illumination from the shape.

Another way to obtain the illumination distribution is first to observe a hemispherical metallic object and then to observe the black pipe directly. The metallic object captures the illumination distribution of the spherical diffuser. This paper only concentrates on proposing a method to estimate the shapes of transparent objects, and further improvement is possible by obtaining the correct illumination distribution.

6.2 Simulation Result

6.2.1 Triangle

Here, we show some results of estimating the 2D shape of simulated objects for evaluating the robustness of our algorithm. The first virtual transparent object is an isosceles triangle whose refractive index is 1.5 and whose two base angles are 76.6 degrees. We render the polarization data of the object observed from an apical angle, and after that, we estimate the front surface shape by using the rendered polarization data as input data. Illumination is distributed uniformly from every direction with the same intensity. The light is not illuminated at the bottom of the shape but is illuminated on the front surface. Illumination distribution, the back surface shape, and the refractive index are given. No noise is added in order to check only the convergence of our method.
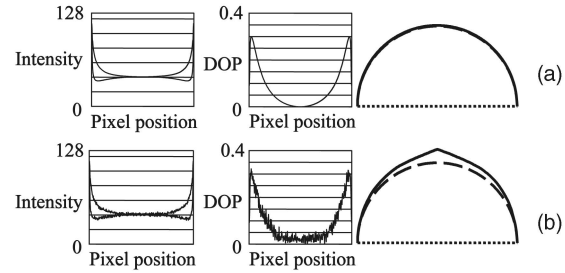
The estimated result is illustrated in Fig. 6. The dashed upper line is the true shape, and the solid line is the estimated shape. The dotted lower line is the back surface, which is given. For each figure, Fig. 6(1) represents the initial state of the shape, and Fig. 6(2) is the resultant shape after 40 iterations. Initial shapes of those in Figs. 6a, 6b, 6c, and 6d are the shapes that are calculated by scaling the true height by 1.8, 1.4, 0.6, and 0.2, respectively. Saito et al.'s method [23] produces two kinds of shapes due to its ambiguity. Initial shapes of those in Figs. 6e and 6f are those two shapes.

The estimated shapes in Figs. 6a, 6b, 6c, and 6e successfully converge to the true shape; thus, we can state that the proposed method is robust in convergence if the proper initial values are set. However, the estimated shapes in Figs. 6d and 6f converge to a different shape from the true shape due to the ambiguity. Our method needs an appropriate initial value to avoid the local minimum made by the ambiguity. Our previous method [16], [18] can solve the ambiguity problem; thus, it is valid to use the shape calculated by our previous method as an initial value.

6.2.2 Hemisphere

The second result is that of a 2D virtual transparent object, which is a hemispherical shape whose refractive index is 1.5. The object is observed from the curved part. First, we analyzed the behavior of our method in the presence of noise. The estimated result is illustrated in Fig. 7. The left of each figure represents the observed intensity, the middle represents the DOP, and the right represents the shape. The upper line of the intensity is I_{max}, and the lower line is I_{min}. The dashed upper line of the shape is the true one, and the solid upper line is the estimated shape. The dotted lower line is the back surface, which is given. Each shape shows the result after 30 iterations. No noise is added for the input intensities in Fig. 7a, and Gaussian noise is added in Fig. 7b. The variance of Gaussian noise we added is 1.0, where the average intensity is about 40.

The surface normal at the center of the object is heading toward the camera; thus, the DOP is zero at these points (Fig. 7a). Recall that the DOP is defined as (17); thus, the non-negative value, DOP, would be greater than 0 if there is a noise in intensity (Fig. 7b). As a result, the surface normal, which should be oriented in the direction of the camera, would incline, and this inclination causes the protruding noise in the center of the object depicted in Fig. 7b. The intensity noise is thought to be caused by the camera noise, the illumination noise, and the object noise. If the illumination is not sufficiently uniform or unpolarized, the illumination noise will occur. The object noise will occur
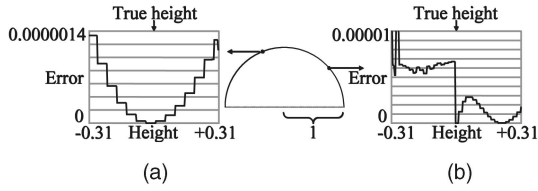
Fig. 8. Cost function of a virtual hemisphere when changing the height: (a) and (b) cost function of a certain surface point.
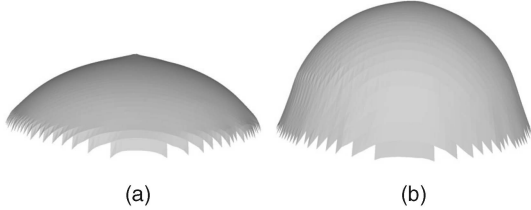

Fig. 9. Estimation result of the hemisphere: (a) initial state (result of previous method) and (b) result after 10 iterations.
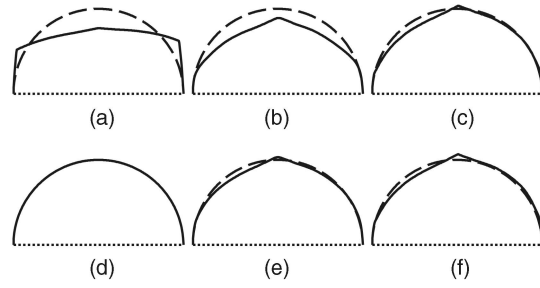

Fig. 10. Estimation result: (a) Initial state (result of previous method). (b) and (c) Results after five and 30 iterations. (d) Initial state (true shape). (e) and (f) Results after five and 30 iterations.
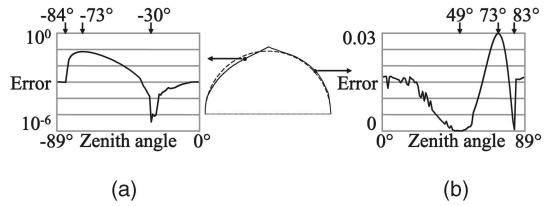

Fig. 11. Cost function of real hemisphere: (a) cost function (logarithmic scale) of a certain surface point and (b) cost function of a certain surface point.

if the smoothness, the transparency, and/or the isotropy of the refractive index are insufficient. Avoiding all of these sources of noise is quite difficult; thus, the shape, especially at the points where the surface normal is heading toward the camera, will cause some errors.

In Section 4, we stated that we do not use (33) for updating the height. Fig. 8 is the cost function if we change the height of a certain point on the object's surface. Though the cost value is zero at the true height, the cost function when changing the height (Fig. 8) is not so smooth, even for simulated data, compared to the cost function when changing the surface normal (Fig. 4 in Section 5.1 and Fig. 11 in Section 6.3.1). Thus, we do not change the height but change the surface normal for updating the shape of the object.

6.3 Measurement Results of Real Object

6.3.1 Hemisphere

For the first measurement result, we observe an acrylic transparent hemisphere from the spherical part, whose refractive index is 1.5 and diameter is 30 mm. We assume that the refractive index and the back surface shape are known. We use the same value for the intensity of the light source, which is obtained in Section 6.1.3.

Fig. 9a represents the result of the previous method [16], [18], [23] and, at the same time, it represents the initial value. Here, the ambiguity is solved manually. Fig. 9b is the result after 10 iterations of our method. The average computation time was 36 [sec] for 1 iteration with 7,854 pixels by using a Pentium 4 3.4-GHz processor. Here, the maximum number of tracings is 10 reflections or transmissions; however, if the energy of the light ray becomes less than a certain threshold, the tracing of the light ray is stopped.

More detailed evaluation is done in the 2D plane that is a cross section of the 3D object, which includes the center of the base circle and the line perpendicular to that circle. The proposed algorithm estimates the front surface shape, a semicircle, by using the polarization data of the 2D plane as input data. The average computation time was 5.9 (sec) for one iteration with 320 pixels. Here, the maximum number of tracings is 100 reflections or transmissions.

The result of applying the proposed method is given in Figs. 10c and 10f. In Fig. 10, the solid line represents the

estimated shape, and the dotted line represents the true shape. For the estimated result shown in Fig. 10c, the result of the previous method [16], [18], [23] (Fig. 10a) is used for the initial state of the shape. For the estimated result shown in Fig. 10f, the true shape, a hemisphere (Fig. 10d), is used for the initial state of the shape. Figs. 10b and 10e and Figs. 10c and 10f are the results after five and 30 iterations, respectively. The shapes converge to a similar shape even if the initial shapes are different. There is a protruding noise at the top of the estimated shape caused by the noise in the input images, as discussed in Section 6.2.2.

In Fig. 11, we show the value of the cost function E_1 (Section 4) of two points at the object's surface. Here, we use the shape after 30 iterations. We virtually modified the zenith angle of the surface normal and calculated the error value for each angle. The horizontal axis in Fig. 11 represents the zenith angle, and the vertical axis represents the value of the cost function.

Fig. 11a is the cost function in a logarithmic scale at the point where the surface normal is heading to the left side of the object, and the true zenith angle is 21.8 degrees. After 30 iterations, our algorithm found the minimum point of the cost function estimated the zenith angle as 29.6 degrees, which is closer to the true value than another local minimum around 84 degrees. These two local minima are caused by the ambiguity problem discussed in our previous paper [16], [18]. Therefore, we have to set an initial value of the zenith angle at less than 73 degrees for this case to avoid the vice local minimum.

Fig. 11b is the cost function at the point where the surface normal is heading to the right side of the object, and the true zenith angle is 48.9 degrees. The estimated zenith angle was 49.4 degrees. The cost function is not smooth enough in some parts; thus, we cannot adopt the methods based on the gradient of cost function such as the steepest descent method or the conjugate gradient method [21]. However, the cost
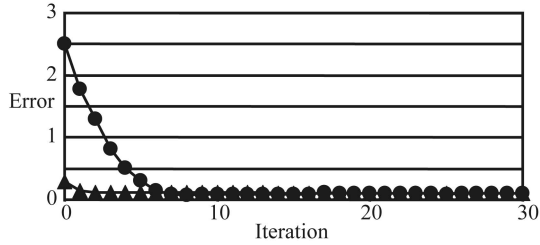
Fig. 12. Error for each iteration. A triangle shows the result when the true shape is the initial value. A circle shows the result when the result of the previous method is the initial value.
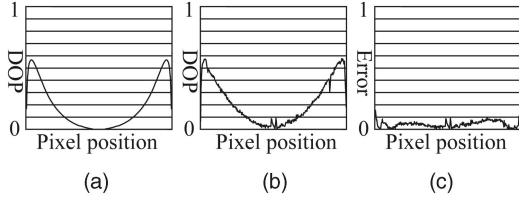

Fig. 13. DOP: (a) computed DOP by polarization raytracing, (b) real DOP, and (c) absolute difference between (a) and (b).

function becomes gradually small while approaching toward the minimum point of the cost function. One-dimensional minimization techniques such as golden section search or Brent's method [21] are less affected by such small disconti- nuity. Therefore, our method, which uses Brent's method, usually finds the correct minimum point.

The value of the cost function (20) per each iteration is plotted in Fig. 12. The vertical axis in Fig. 12 represents the value of (20), whereas the horizontal axis represents the iteration number. A circle mark is the value of the result whose initial state is the result of the previous method [16], [18], [23]. A triangle mark is the value of the result whose initial state is the true shape. The leftmost value is the value of the cost function of the initial state. Both the value and the shape did not change after around eight iterations.

The root mean square (RMS) error between the estimated value and the true value is used to compare the accuracy between the proposed method and the previous method [16], [18], [23]. The RMS error of the surface normal was 23.3 degrees for the previous method, 9.30 degrees for our method when the initial state was the result of the previous method, and 9.31 degrees for our method when the initial state was the true shape. The RMS error of the height was 2.70 mm for the previous method, 0.755 mm for our method when the initial state was the result of the previous method, and 0.605 mm for our method when the initial state was the true shape.

Fig. 13a is the graph of the DOP calculated by using the polarization raytracing method with the true hemispherical shape. Fig. 13b is the graph of the DOP obtained by observing the real transparent hemisphere. Fig. 13c is the graph of the absolute difference between the values in Fig. 13a and the values in Fig. 13b. The horizontal axis in Figs. 13a, 13b, and 13c represents the pixel position. The vertical axis in Figs. 13a and 13b represents the DOP, and the vertical axis in Fig. 13c represents the error. Two peaks in the middle of the object cause the error. Such peaks are caused by the noise in the input images discussed in Section 6.2.2 and are difficult to
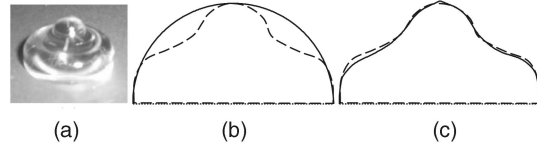

Fig. 14. Bell-shaped transparent acrylic real object: (a) real image, (b) initial value, and (c) result after 30 iterations.

avoid. This means that even if the iterative computation tries hard to minimize the error, the estimated shape can never attain the true shape due to this error in the input data.

6.3.2 Bell-Shaped Object

Next, we observe the transparent object shown in Fig. 14a. This object is made of acrylic and is a body of revolution. Its refractive index is 1.5 and its diameter at the base is 24 mm. The object is observed from its projected area. The front surface is a curved surface and the back surface is a disk. The camera is set orthogonally to the disk. We assume that the refractive index and the back surface shape are known. We use the same value for the intensity of the light source that is obtained in Section 6.1.3.

We estimate the shape of a cross section of the object to analyze the precision of the proposed method. The cross section includes the center of the base circle and the line perpendicular to that circle. The initial value is set to be a semicircle shown in Fig. 14b. The estimated shape after 30 iterations is illustrated in Fig. 14c. RMS of the height was 0.31 mm. The solid curve represents the obtained front shape, and the dashed line represents the true shape. The true shape was obtained from the silhouette extracted manually by a human operator from the photograph of the object taken from the side.

6.3.3 Dog-Shaped Object

Finally, we observe a dog-shaped object shown in Figs. 15a and 15b and Fig. 16b. This object is made of glass, and its refractive index is 1.5. The object is observed from the opposite direction to the planar base. The camera is set orthogonally to the plane. We assume that the refractive index and the back surface shape are known. We use the same intensity value for light sources obtained in Section 6.1.3.

We use the shape obtained manually by human operation as an initial value for the experiment, which is shown in Figs. 15c and 15d. The estimation results after 10 iterations are shown in Figs. 15e and 15f. Notice that the curvature of the dog's neck is improved by our method. This result demon- strates that our method can also estimate the shape of the concave part of the object, which causes strong interreflec- tions. The shape of the dog's tail is not well estimated because

1. the initial value was not properly set for the tail;
2. the tail, which protrudes from the body, has a sharp feature that the method cannot deal with; and
3. the tail violates Assumption 6 in Section 2, that is, there is a "jump" at the tail when observed from the top.

The shape of the top of the head is not also good due to the noise in input images, as discussed in Section 6.2.2.

Fig. 16b represents the ambiguity problem discussed in Section 5.1. The shape shown in Figs. 15e and 15f is used to
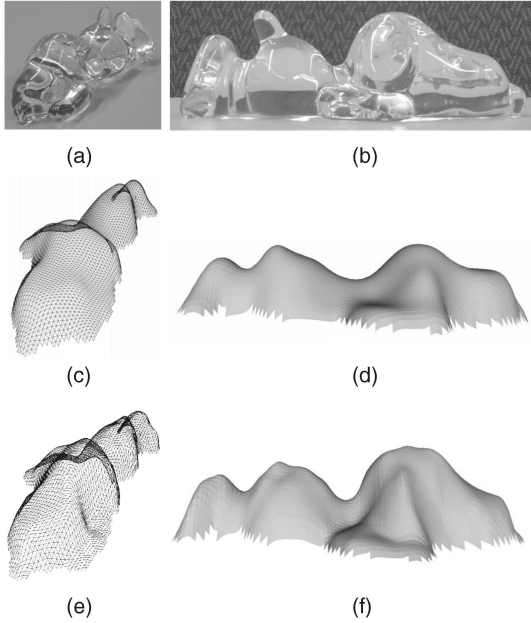
Fig. 15. Dog-shaped glass object: (a) and (b) real image, (c) and (d) initial state of the shape given manually, and (e) and (f) estimated shape after 10 iterations.
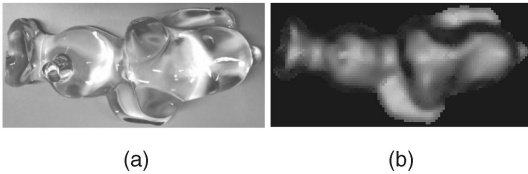

Fig. 16. Ambiguity of dog-shaped glass object: (a) real image and (b) ambiguity (white: large ambiguity and black: small ambiguity).

calculate the ambiguity. The ambiguity value is represented by the angle between two zenith angles calculated from the DOP. In Fig. 16b, the black area represents no ambiguity, which means that the angle between the two surface normals is zero. The white area represents the highest ambiguity, 90 degrees between two angles, which means that one of the surface normals is heading toward the camera, and the other is heading vertically to the camera direction. If the ambiguity is almost zero, we can uniquely determine the surface normal. If the ambiguity is almost 90 degrees, the algorithm can easily find the correct surface normal even if the initial surface normal is largely set apart from the correct one, although the initial surface normal must be closer to the correct one than to the wrong one. In an actual situation, it is difficult to know how close the initial shape should be to the true shape in order to estimate the shape successfully.

6.4 Comparison to Other Research

In the above sections, we have compared our results to those obtained with the previous methods [16], [18], [23]. In this section, we will compare the proposed method to other researchers' methods. Other researchers have also proposed methods to estimate the shape of transparent objects. Murase's method [20] can only measure the shape of a water surface. Ben-Ezra and Nayar's method [3] can only measure a parameterized surface such as a sphere or rounded cube.
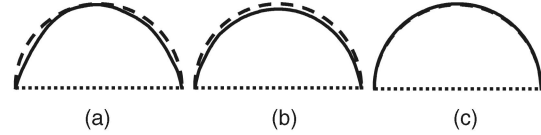

Fig. 17. Comparison between Hata et al.'s method and the proposed method: (a) initial shape, (b) result of Hata et al.'s method, and (c) result of the proposed method.

Hata et al.'s method [8] is suitable for measuring pastelike shapes; however, the method can possibly be used to estimate an arbitrary shape. Therefore, this method is of particular interest and deserves comparison with our method. Recently, Kutulakos et al. [15], [19] proposed a method that can measure an arbitrary shape. In most cases, their method produces a better shape than Hata et al.'s method by observing the object from multiple directions. Our proposed method and Hata et al.'s method observe the object from a single viewpoint; thus, we compare the proposed method with Hata et al.'s method for fair comparison.

6.4.1 Hata et al.'s Algorithm

First, we will briefly explain Hata et al.'s algorithm. The target object is set on a desk, and the camera observes the transparent object from above. A slit ray beam is shot from the projector to the object. The object, camera, and projector are fixed. Multiple images are taken for each shot of the slit ray beam. The cost function is the difference of the position of the slit ray beam on the desk between the observed position and the calculated position. Computation of the shape is done by using a genetic algorithm.

6.4.2 Comparison to the Proposed Method

The evaluation is done in computer simulation because the two methods must be compared with the estimation algorithm itself without depending on the accuracy of the measurement apparatus. Evaluation is done in a 2D plane. The number of pixels we used was 320 points. The number of slit ray beams we used for Hata et al.'s method was 320 lights. The projector was set 30 degrees right to the camera. No noise was added so that we could compare only the convergence of these two algorithms.

We applied Hata et al.'s method and our proposed method to the virtual transparent hemisphere (semicircle) presented in Fig. 17. Fig. 17a is one of the initial shapes generated by Hata et al.'s method. We used the same shape also for the proposed method. Figs. 17b and 17c are the estimation results of Hata et al.'s method and the proposed method, respectively, after 50 iterations. The solid line represents the estimated shape, the upper dashed line represents the true front shape, and the lower dotted line represents the back surface shape given both for Hata et al.'s method and the proposed method. Hata et al.'s method cannot estimate the shape of the hemisphere, whereas the proposed method successfully estimates it. The RMS error of surface normal in Hata et al.'s method was 2.3 degrees, whereas that in the proposed method was 0.3 degrees.

7   CONCLUSION

In this paper, we have proposed a novel method for estimating the surface shape of transparent objects by minimizing the difference between the input polarization data taken by observing the transparent object and the computed polarization data rendered by the polarization raytracing method. Though there are some assumptions to be satisfied for the proposed method, experimental results verify that we can estimate the shapes of many kinds of transparent objects when the assumptions are satisfied, and the initial value of the shape is properly given.

Often, artificial transparent objects have a planar base that enables them to stand by themselves. Also, the material (refractive index) of the artificial transparent objects is known in many cases. Thus, the assumption we adopted in this paper, "back surface shape and refractive index are known," is effective in many cases. However, not all objects meet these conditions; thus, we intend to exploit a method that can measure the back surface shape and refractive index at the same time, as well as the front surface shape.

The target object must be sufficiently small compared to the spherical diffuser; thus, large objects are not measurable. Therefore, we intend to apply our method without using the spherical diffuser and the light sources: measurement is also possible in both indoor and outdoor environments if the intensity and the polarization state of the surrounding environment are acquired beforehand.

The input polarization data is polluted by some noise due to the variation of the refractive index inside the object or the opacity of the object. In order to reduce such noise practically, multiple input data are needed, taken under different illumination or taken from different directions.

Possible application fields for the modeling of transparent objects can range from computer-aided manufacturing to classifying rubbish for recycling glass and plastic bottles, creating 3D catalogs for online shopping, and modeling beautiful glass objects of art that are hard but fragile. Our basic technique for modeling the surface shape of transparent objects is the first step in this wide area of applications.

ACKNOWLEDGMENTS

REFERENCES

[1]   G.A. Atkinson and E.R. Hancock, "Recovery of Surface Orientation from Diffuse Polarization," *IEEE Trans. Image Processing,* vol. 15, no. 6, pp. 1653-1664, 2006.
[2]   G.A. Atkinson and E.R. Hancock, "Polarization-Based Surface Reconstruction via Patch Matching," *Proc. IEEE CS Conf. Computer Vision and Pattern Recognition,* pp. 495-502, 2006.
[3]   M. Ben-Ezra and S.K. Nayar, "What Does Motion Reveal about Transparency?" *Proc. IEEE Int'l Conf. Computer Vision,* pp. 1025-1032, 2003.
[4]   M. Born and E. Wolf, *Principles of Optics,* p. 803. Pergamon Press, 1959.
[5]   R.A. Chipman, "Mechanics of Polarization Ray Tracing," *Optical Eng.,* vol. 34, no. 6, pp. 1636-1645, 1995.
[6]   R. Courant and D. Hilbert, *Methods of Mathematical Physics,* p. 577. John Wiley & Sons, 1953.
[7]   S. Guy and C. Soler, "Graphics Gems Revisited: Fast and Physically-Based Rendering of Gemstones," *ACM Trans. Graphics,* vol. 23, no. 3, pp. 231-238, 2004.
[8]   S. Hata, Y. Saitoh, S. Kumamura, and K. Kaida, "Shape Extraction of Transparent Object Using Genetic Algorithm," *Proc. Int'l Conf. Pattern Recognition,* pp. 684-688, 1996.
[9]   E. Hecht, *Optics,* p. 698. Addison-Wesley, 2002.
[10]   B.K.P. Horn, *Robot Vision,* p. 509. MIT Press, 1986.
[11]   B.K.P. Horn, "Height and Gradient from Shading," *Int'l J. Computer Vision,* vol. 5, no. 1, pp. 37-75, 1990.
[12]   K. Ikeuchi and B.K.P. Horn, "Numerical Shape from Shading and Occluding Boundaries," *Artificial Intelligence,* vol. 17, pp. 141-184, 1981.
[13]   K. Ikeuchi, "Reconstructing a Depth Map from Intensity Maps," *Proc. Int'l Conf. Pattern Recognition,* pp. 736-738, 1984.
[14]   K. Koshikawa and Y. Shirai, "A Model-Based Recognition of Glossy Objects Using Their Polarimetrical Properties," *Advanced Robotics,* vol. 2, no. 2, pp. 137-147, 1987.
[15]   K.N. Kutulakos and E. Steger, "A Theory of Refractive and Specular 3D Shape by Light-Path Triangulation," *Proc. IEEE Int'l Conf. Computer Vision,* pp. 1448-1457, 2005.
[16]   D. Miyazaki, M. Saito, Y. Sato, and K. Ikeuchi, "Determining Surface Orientations of Transparent Objects Based on Polarization Degrees in Visible and Infrared Wavelengths," *J. Optical Soc. Am. A,* vol. 19, no. 4, pp. 687-694, 2002.
[17]   D. Miyazaki, R.T. Tan, K. Hara, and K. Ikeuchi, "Polarization-Based Inverse Rendering from a Single View," *Proc. IEEE Int'l Conf. Computer Vision,* pp. 982-987, 2003.
[18]   D. Miyazaki, M. Kagesawa, and K. Ikeuchi, "Transparent Surface Modeling from a Pair of Polarization Images," *IEEE Trans. Pattern Analysis and Machine Intelligence,* vol. 26, no. 1, pp. 73-82, Jan. 2004.
[19]   N.J.W. Morris and K.N. Kutulakos, "Dynamic Refraction Stereo," *Proc. IEEE Int'l Conf. Computer Vision,* pp. 1573-1580, 2005.
[20]   H. Murase, "Surface Shape Reconstruction of a Nonrigid Transparent Object Using Refraction and Motion," *IEEE Trans. Pattern Analysis and Machine Intelligence,* vol. 14, no. 10, pp. 1045-1052, Oct. 1992.
[21]   W.H. Press, S.A. Teukolsky, W.T. Vetterling, and B.P. Flannery, *Numerical Recipes in C: The Art of Scientific Computing,* p. 994. Cambridge Univ. Press, 1992.
[22]   S. Rahmann and N. Canterakis, "Reconstruction of Specular Surfaces Using Polarization Imaging," *Proc. IEEE CS Conf. Computer Vision and Pattern Recognition,* pp. 149-155, 2001.
[23]   M. Saito, Y. Sato, K. Ikeuchi, and H. Kashiwagi, "Measurement of Surface Orientations of Transparent Objects by Use of Polarization in Highlight," *J. Optical Soc. Am. A,* vol. 16, no. 9, pp. 2286-2293, 1999.
[24]   Y.Y. Schechner, J. Shamir, and N. Kiryati, "Polarization and Statistical Analysis of Scenes Containing a Semireflector," *J. Optical Soc. Am. A,* vol. 17, no. 2, pp. 276-284, 2000.
[25]   D.C. Tannenbaum, P. Tannenbaum, and M.J. Wozny, "Polarization and Birefringency Considerations in Rendering," *Proc. ACM Ann. Conf. Computer Graphics,* pp. 221-222, 1994.
[26]   A. Wilkie, R.F. Tobler, and W. Purgathofer, "Combined Rendering of Polarization and Fluorescence Effects," *Proc. Eurographics Workshop Rendering,* pp. 197-204, 2001.
[27]   L.B. Wolff and D.J. Kurlander, "Ray Tracing with Polarization Parameters," *IEEE Computer Graphics and Applications,* vol. 10, no. 6, pp. 44-55, 1990.
[28]   L.B. Wolff and T.E. Boult, "Constraining Object Features Using a Polarization Reflectance Model," *IEEE Trans. Pattern Analysis and Machine Intelligence,* vol. 13, no. 7, pp. 635-657, July 1991.

Daisuke Miyazaki received the BS degree in science in 2000, the MS degree in information science and technology in 2002, and the PhD degree in information science and technology in 2005, all from the University of Tokyo. He is a postdoctoral researcher at the University of Tokyo, Japan. He received the Best Overall Paper Award from the International Conference on Virtual Systems and Multimedia (VSMM) in 2000. He is a member of the IEEE and the IEEE Computer Society.

Katsushi Ikeuchi received the BEng degree in mechanical engineering from Kyoto University, Kyoto, Japan, in 1973 and the PhD degree in information engineering from the University of Tokyo, Japan, in 1978. He is a professor at the Interfaculty Initiative in Information Studies, University of Tokyo, Japan. After working at the AI Laboratory at the Massachusetts Institute of Technology for three years, the Electrotechnical Laboratory for five years, and the School of Computer Science at Carnegie Mellon University for 10 years, he joined the University of Tokyo in 1996. He was selected as a distinguished lecturer of the IEEE Signal Processing Society for the period of 2000-2001 and a distinguished lecturer of the IEEE Computer Society for the period of 2004-2006. He has received several awards, including the David Marr Prize in International Conference on Computer Vision (ICCV) 1990, IEEE R&A K.-S. Fu Memorial Best Transaction Paper Award in 1998, and the best paper awards in International Conference on Computer Vision and Pattern Recognition (CVPR) 1991, International Conference on Virtual Systems and Multimedia (VSMM) 2000 and 2004. In addition, in 1992, his paper, "Numerical Shape from Shading and Occluding Boundaries," was selected as one of the most influential papers to have appeared in the *Artificial Intelligence Journal* within the past 10 years. He is a fellow of the IEEE.

▷ **For more information on this or any other computing topic, please visit our Digital Library at** www.computer.org/publications/dlib.